JOURNAL OF GEOPHYSICAL RESEARCH, VOL. 116, D02209, doi:10.1029/2010JD014510, 2011

Aerosol closure study by lidar, Sun photometry, and airborne optical counters during DAMOCLES field campaign at El Arenosillo sounding station, Spain

J. L. Guerrero-Rascado,[1,2,3] J. Andrey,[4] M. Sicard,[5] F. Molero,[6] A. Comerón,[5] M. Pujadas,[6] F. Rocadenbosch,[5] R. Pedrós,[7] O. Serrano-Vargas,[8] M. Gil,[4] F. J. Olmo,[2,3] H. Lyamani,[2,3] F. Navas-Guzmán,[2,3] and L. Alados-Arboledas[2,3]

Received 18 May 2010; revised 27 October 2010; accepted 11 November 2010; published 26 January 2011.

[1] We present a comparison of aerosol properties derived from in situ and remote sensing instruments during DAMOCLES campaign, aimed at investigating the equivalence between the instrumentation and methodologies employed by several Spanish groups to study atmospheric aerosols at a regional background site. The complete set of instruments available during this closure experiment allowed collecting a valuable high-resolution aerosol measurement data set. The data set was augmented with airborne in situ measurements carried out in order to characterize aerosol particles during the midday of 29 June 2006. This work is focused on aerosol measurements using different techniques of high-quality instruments (ground-based remote sensing and aircraft in situ) and their comparisons to characterize the aerosol vertical profiles. Our results indicate that the variability between the detected aerosol layers was negligible in terms of aerosol optical properties and size distributions. Relative differences in aerosol extinction coefficient profiles were less than 20% at 355 and 532 nm and less than 30% at 1064 nm, in the region with high aerosol concentration. Absolute differences in aerosol optical depth (AOD) were below 0.01 at 532 and 1064 nm and less than 0.02 at 355 nm, less than the uncertainties assumed in the AOD obtained from elastic lidar. Columnar values of the lidar ratio revealed some discrepancies with respect to the in situ aircraft measurements, caused fundamentally by the lack of information in the lowest part of the boundary layer.

Citation: Guerrero-Rascado, J. L., et al. (2011), Aerosol closure study by lidar, Sun photometry, and airborne optical counters during DAMOCLES field campaign at El Arenosillo sounding station, Spain, *J. Geophys. Res.*, *116*, D02209, doi:10.1029/2010JD014510.

1. Introduction

[2] Aerosol particles affect the radiative energy budget of the Earth-atmosphere system by scattering solar radiation and absorbing solar and terrestrial infrared radiation. At present instrumentation such as lidars and Sun photometers have become powerful tools to detect aerosols during relevant episodes as Saharan and Asian mineral dust outbreaks and volcanic eruptions and are and will continue to be in the future a key for the long-term monitoring of aerosols over the world. Therefore monitoring networks of passive and active remote sensors such as AERONET [*Holben et al.*, 1998], EARLINET [*Bösenberg et al.*, 2001], and MPLNET [*Welton et al.*, 2001] increase continuously their relevance.

[3] Different aspects control the effect of the atmospheric aerosol over Earth's radiation budget. In this sense, the atmospheric aerosol radiative forcing strongly depends on the surface albedo. Thus depending on the type of aerosol and the underlying surface (land or ocean), the magnitude and sign of the radiative forcing can be modified drastically. Knowledge of the aerosol vertical distribution can be relevant for several reasons. The vertical distribution of aerosols modifies the vertical profile of heating rate, changing the atmospheric stability, and thus influencing convective processes and clouds [e.g., *Ackerman et al.*, 2000; *Quijano et al.*, 2000; *Won et al.*, 2004; *McFarquhar and Wang*, 2006; *Ramanathan et al.*,

[1]Centro de Geofísica de Évora, Universidad de Évora, Évora, Portugal.
[2]Departamento de Física Aplicada, Facultad de Ciencias, Universidad de Granada, Granada, Spain.
[3]Centro Andaluz de Medio Ambiente, Junta de Andalucía-Universidad de Granada, Granada, Spain.
[4]Área de Investigación e Instrumentación Atmosférica, Instituto Nacional de Técnica Aeroespacial, Torrejón de Ardoz, Spain.
[5]Remote Sensing Laboratory, Institut d'Estudis Espacials de Catalunya, Barcelona, Spain.
[6]Centro de Investigaciones Energéticas, Medioambientales y Tecnológicas, Madrid, Spain.
[7]Departamento de Física de la Tierra y Termodinámica, Universidad de Valencia, Valencia, Spain.
[8]Área de Ensayos en Vuelo y Armamento, Instituto Nacional de Técnica Aeroespacial, Torrejón de Ardoz, Spain.

0148-0227/11/2010JD014510

Table 1. List of Instruments Involved in the DAMOCLES Field Campaign

Measurement Type	Instrument	Model	Number	Used in This Work
In situ	High volume collectors	DIGITEL	1	-
		MCV	1	
	Nephelometer	TSI-3563	3	yes
	Aerodynamic particle sizer	APS 3321	2	yes
	Multi angle absorption photometer	MAAP 5012	1	yes
	Scanning mobility particle sizer	SMPS 3936	1	-
	Grimm spectrometer	GRIMM 190	1	-
Column	Sun photometer	CIMEL CE318	7	yes
Range-resolved	Lidar	lab. lidars	2	-
		LR321D400	1	yes
		CAML CE370-2	1	-
	Airborne particle sized	PCASP-100X	1	yes
	Forward scattering spectrometer probe	FSSP-100-ER	1	-
	Radiosoundings		2/day	yes

2007]. Furthermore, it is important to know the vertical distribution to understand and/or model the radiative effect. Particularly, the vertical distribution of aerosols which have strong absorption of shortwave radiation influence the radiative effect at the top of atmosphere [e.g., *Haywood and Ramaswamy*, 1998; *Meloni et al.*, 2005; *Gadhavi and Jayaraman*, 2006]. Additional aspects of the atmospheric aerosols to be considered include the quantification of the aerosol direct effect in the thermal infrared and in cloudy conditions. In this sense, the current estimates of the warming effects in this spectral range remain highly uncertain, because of lack of observations of vertically resolved aerosol information [*Sokolik et al.*, 2001].

[4] Knowledge of vertical distribution can be achieved via several approaches. Remote sensing techniques such as lidar, both ground-based and satellite-based such as CALIPSO, are devoted to long-term monitoring of aerosol optical properties. Aircraft in situ measurements, on the other hand, although limited in time can be used to study aerosol properties during intensive field campaigns in order to assess the applicability of the lidar techniques. Closure experiments offer the opportunity to explore aerosol properties based on an overdetermined data set of measurements using different techniques.

[5] The Determinación de Aerosoles por Medidas Obtenidas en Columna (Lidar y Extinción) y Superficie (DAMOCLES) thematic network was conceived as an interdisciplinary study of atmospheric aerosol particles, including emissions, dynamics, physical and chemical properties, radiative effects, and their interaction with clouds [*Pey et al.*, 2008; *Estellés et al.*, 2009; J. A. Martinez-Lozano et al., Intercomparison of instrumentation of atmospheric aerosol measurements, paper presented at European Aerosol Conference, Eur. Aerosol Assem., Salzburg, Austria, 2007]. The DAMOCLES field campaign was designed to compare the instrumentation and methodology employed by several Spanish groups at a regional background site in the Southwestern coast of Spain [*Pey et al.*, 2008]. The campaign was conducted from 28 June to 5 July 2006 at the Atmospheric Sounding Station ESAt-El Arenosillo (37.11°N, 6.73°W, 0 a.s.l.) operated by the National Institute of Aerospace Technology (INTA).

[6] The array of instruments used in this closure experiment provided a high-resolution aerosol measurements data set. Moreover, aerosol particles were studied by airborne in situ measurements around midday on 29 June. This data set obtained during DAMOCLES field campaign enables to analyze the agreement of in situ and remote sensing techniques to characterize the vertical distribution of aerosol properties in conditions of optimized proximity between the ground lidar and the aircraft track.

[7] The subject of this paper is the comparison of the major properties of aerosol particles as optical and microphysical properties derived both from aircraft and ground-based remote sensing. This work complements the previous studies on analysis made with ground-based active and passive remote sensing and in situ techniques during DAMOCLES field campaign. The paper is organized as follows. Sections 2 and 3 describe the instrumentation and methods. Section 4 focuses on the meteorological conditions which prevailed during the case study, on the vertical structure of the atmosphere, and on the comparison of lidar, aircraft, and photometric data. Finally, Section 5 presents the main conclusions of this work.

2. Instrumentation

[8] The whole set of instruments is listed in Table 1 but only the instrumentation used in this work is described in detail. From the point of view of column integrated data, aerosol particles were characterized using seven Cimel CE-318 Sun photometers. To characterize aerosol particles, in situ high volume collectors (DIGITEL and MCV) were used for PM10, PM2.5, and PM1, with two cascade impactors for particulate matter measurements in 7–8 granulometric fractions. In addition, three integrating nephelometers (model TSI-3563), two aerodynamic particle sizers (APS, model 3321), a multiangle absorption photometer (MAAP, model 5012), a scanning mobility particle sizer (SMPS, model 3936), and a Grimm spectrometer (model 190) were used. From the point of view of vertical profiling of atmosphere, several tools were available. Meteorological radio soundings were performed twice per day to characterize the atmospheric conditions prevailing at El Arenosillo. An aircraft managed by the National Institute of Aerospace Technology (INTA) held airborne sensors to measure meteorological parameters and Passive Cavity Aerosol Spectrometer (PCASP) to analyze aerosol particle size distributions. The vertical distribution of aerosol optical properties were obtained by means of lidar technique using four

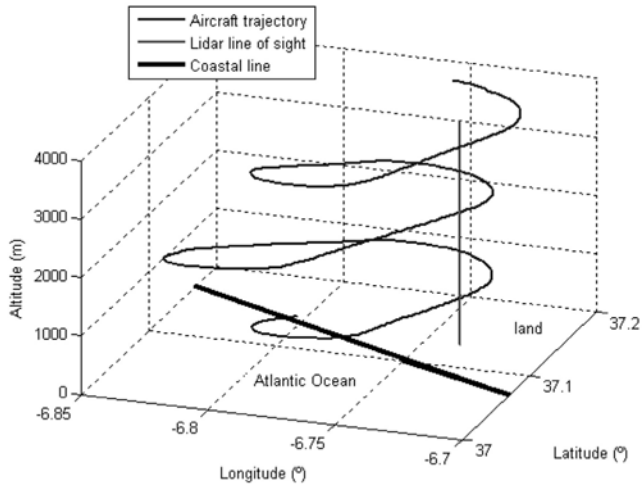

Figure 1. Descent flight track for DAMOCLES campaign based in El Arenosillo station, Spain.

systems, all of them included in the Spanish and Portuguese Aerosol Lidar Network (SPALINET). The intercomparison of the lidar systems operated during DAMOCLES field campaign has been analyzed in a previous work [*Sicard et al.*, 2009]. In this work, data measured by the Raman lidar LR321D400 has been employed because of its multiwavelength capabilities.

[9] Airborne measurements were carried out by the INTA CASA C-212-200 atmospheric aircraft. This aircraft was designed as a light military transport aircraft and was modified for atmospheric research. Measurements of temperature, dew point, pressure, GPS position, and aerosol size distribution were performed during DAMOCLES campaign. A Passive Cavity Aerosol Spectrometer Probe model 100X (PCASP-100X) and Forward Scattering Spectrometer Probe model 100-ER (FSSP-100-ER) were used for aerosol size distribution. Both probes have been designed by Particle Measuring Systems Inc. (PMS). The instruments were fixed at two hard points located under the aircraft wings.

[10] The PCASP instrument was mounted onto the INTA-C212 aircraft which flew on 29 June 2006, overflying the Atmospheric Sounding Station ESAt-El Arenosillo. The airborne platform developed two vertical profiles following a pseudospiral centered at ESAt and having a radius of about 7.5 km. Maximum height reached was 4.1 km (a.s.l.) at 1027 UTC. A gentle ascent and descent rate was used of about 3.75 m/s in order to increase vertical resolution. Straight and level runs were performed at various altitudes within the different aerosol layers, mainly over land but sometimes the aircraft was over ocean. Figure 1 shows the descending track (which lasted 17 min) of the INTA-C212 aircraft during this flight. The aircraft overpass around the lidar systems was performed at several altitudes between 0.25 and 4.1 km within the aerosol layers.

[11] The C212 aircraft requires a pitch angle (angle between velocity vector and aircraft axis) near 4° or 5° to ascend. Under this condition, the instrumentation devoted to measure aerosol size distribution (PCASP-100X) does not operate well [*Haywood et al.*, 2003] so ascent data have been rejected. Descent profile data have been used to retrieve optical properties because pitch angle can be kept near zero and it is possible to obtain an optimum measurement.

[12] PCASP sizes the aerosol by illuminating the particle and collecting the light scattered into a fixed solid angle. This system is based on a He:Ne laser source at 632.8 nm, and light scattered by the particles is collected and classified into one of 15 size channels in the range from 0.1 to 3.0 mm diameter [*Fiebig et al.*, 2002]. The relation of scattering cross section and particle diameter at the channel limits depends on the particle refractive index and the particle shape. If the refractive index of the sampled particles is different from the calibration particle refractive index, the channel limits are corrected by applying the Mie theory. PCASP partially dries the sample before it is sized due to deceleration in the inlet cone, and due to focusing of the sample into the laser beam with dried sheath air. As a result of this drying process, relative humidity of the sample is lower than 40% [*Strapp et al.*, 1992]. A good agreement between aerosol size distributions from FSSP-300 and PCASP-100X [*Strapp et al.*, 1992] has been found at relative humidity near 40%. The measurement uncertainties associated with the PCASP have been discussed by a number of authors [e.g., *Kim and Boatman*, 1990; *Strapp et al.*, 1992] as have those of the FSSP-100 and FSSP-300 [*Baumgardner et al.*, 1985, 1992; *Baumgardner and Spowart*, 1990]. Accuracy on size characterization and aerosol concentration are 16% and 20% respectively [*Baumgardner et al.*, 2005]. PCASP heater was switch off during the flight.

[13] The Raman lidar LR321D400 (Raymetrics S.A., Greece) is a compact and robust mobile system that was operated at ground level during DAMOCLES field campaign. It operates with a Nd:YAG laser at the fundamental wavelength of 1064 nm and second and third harmonics at 532 and 355 nm, respectively. Pulses at these wavelengths are emitted simultaneously with a 10 Hz repetition rate and energy levels between 60 and 110 mJ. The optical receiver is based on a Cassegrainian design with primary and secondary mirrors of 400 mm and 9 mm diameter. Photomultipliers tubes are used to detect the backscattered signal in analog and photon counting modes at 532 (considering depolarization) and 355 nm. An avalanche photodiode is used to detect analog signal at 1064 nm. For nighttime operation, the system is equipped with Raman channels detection at 387 and 408 nm (Raman shifted signal by nitrogen molecules and water vapor, respectively). Optimum spatial resolution at all wavelengths is 7.5 m.

[14] The Sun photometer Cimel CE-318 is the standard Sun/sky photometer used in the AERONET network [*Holben et al.*, 1998]. The Cimel CE-318 is a Sun photometer which makes direct sun measurements with a 1.2° full field of view every 15 min at 340, 380, 440, 675, 870, 940, and 1020 nm. The instrument includes protocols for the measurements of sky radiance values at 440, 675, 840, and 1020 nm using the so-called almucantar and principal plane geometries. A full description can be seen in the work of *Holben et al.* [1998]. Two kinds of calibrations are required for the instrument, one for the direct irradiance and one for the sky radiance. The direct irradiance is calibrated using the Langley method at a high mountain site in the close range of Sierra Nevada (2200 m a.s.l) at least twice a year [*Alcántar-Ruiz et al.*, 2004]. The subsystem that measures the radiances is cali-

brated at the laboratory using an integrating sphere [*Alados-Arboledas et al.*, 2004, 2008].

[15] The integrating nephelometer (TSI, model 3563) draws the ambient air through a temperature-monitored inlet at a flow rate of 30 l min^{-1}, illuminates the sample with a halogen lamp, and measures scattered light at 450, 550, and 700 nm using three photomultiplier tubes. The scattered light is integrated over an angular range of 7–170° from the forward direction. Using the backscatter shutter, this range can be adjusted to either 7–170° or 90–170° to give total scatter and backscatter signals. Pressure and temperature are measured in the scattering chamber and used to calculate scattering by air molecules, which is then subtracted from total scattering to determine scattering by aerosol particles. Calibration of the nephelometer was carried out every three months using CO_2 as a high span gas and filtered air as a low span gas.

[16] The multiangle absorption photometer (MAAP) (Thermo ESM Andersen Instruments, Erlangen, Germany) performs absorption measurements. In this instrument, particles are deposited on a quartz fiber filter. A continuous 670 nm laser illuminates the filter matrix perpendicularly and simultaneous measurements are made of radiation penetrating through the filter and the radiation scattered back at two detection angles. In the MAAP the determination of the aerosol absorption coefficient of the deposited aerosol uses radiative transfer calculations and explicitly includes a treatment of scattering effects from the filter matrix and the light scattering aerosol component. The particle-loaded filter is treated as a two-layer system: the aerosol-loaded layer of the filter and the particle-free filter matrix. Radiative processes inside the layer of deposited aerosol and between this layer and the particle-free filter matrix are taken into account separately.

[17] An aerodynamic aerosol sizer (APS-3321, TSI) is used to measure the particle size distributions. This instrument is an optical particle counter that measures particle diameter and aerosol number density, in real time, in 52 nominal size bins in the aerodynamic diameter range 0.50–20 mm by determining the time of flight of individual particles in an accelerating flow field. The APS can measure number densities up to 1000 particles/cm^3 at 0.5 and 10 mm diameters with coincidence errors inferior to 5% and 10%, respectively. The minimum and maximum number densities that this instrument can measure are 0.001 and 10,000 particles/cm^3, respectively. For solid particles, counting efficiencies range from 85% to 99% [*Volckens and Peters*, 2005]. The APS was operated at flow rate of 5 l min^{-1} and an averaging time of 5 min.

3. Methodology

3.1. PCASP-100X Probe and Flight Description

[18] Aerosol optical properties can be determined by means of "in situ" aircraft instrumentation. Aerosol optical properties profiles are calculated by applying the Mie theory [*Bohren and Huffman*, 1983] to the sampled size distribution. The application of Mie theory may be an additional source of error when the non-sphericity of particles is relevant. However, as we discuss in section 4, the particles found in this work show small sizes and the assumption of spheres is plausible. Thus the aerosol extinction and backscatter coefficient as a function of altitude *z* are given by

$$\delta(z;\ \text{Þ} = \sum_{i=1}^{15} r^2 Q_e(m; x_i \text{Þ} N_i(z \text{Þ} \qquad (1\text{Þ}$$

$$j3(z;\ \text{Þ} = \sum_{i=1}^{15} r^2 Q_b(m; x_i \text{Þ} N_i(z \text{Þ} \qquad (2\text{Þ}$$

where a is the aerosol extinction coefficient, b is the aerosol backscatter coefficient, r_i is the geometrical radius or Stokes radius of the particle for the i channel, Q_e and Q_s are the extinction and backscatter efficiencies, respectively, computed by means of Mie theory, m is the complex refractive index of aerosol particles, x_i is the size parameter defined as $x_i = 2\pi r_i/\lambda$, and N_i is the number of particles measured at the i channel. Similar procedures have been applied recently to dust particles researched during SAMUM [i.e., *Weinzierl et al.*, 2009]. Particles with sizes lower than the particle radius corresponding to the first channels can be neglected because their backscatter and extinction efficiencies are almost zero. For computational purpose and after validation of our analysis it has been assumed a posteriori that no particles larger than those collected by the last PCASP channel (d_{15} = 2.47 mm) were present. PCASP system provides the optical equivalent radius that is converted into aerodynamic radius after calibration using monodisperse polystyrene latex spheres (m = 1.58 ± 0i). Then, the aerodynamic radius is related to geometrical one by the following equation [*Binnig et al.*, 2007]:

$$r_{St} = \sqrt{\frac{\chi}{\rho}}\, r_{ae} \qquad (3\text{Þ}$$

where r_{St} and r_{ae} are the geometrical radius (or Stokes radius) and the aerodynamic radius, respectively, r is the particle density, and c is the shape factor of particles, that takes into account nonspherical features of the aerosol particles.

[19] From these data, the aerosol optical depth (AOD), which takes into account the attenuation of radiation when is propagated through the atmospheric aerosol, is obtained by integrating the extinction profile. The FSSP performance was out of reliable limits so its data have not been used in this work.

3.2. Raman Lidar LR321D400

[20] The Raman lidar permits profiling of the aerosol optical properties. Only profile segments not corrupted by overlap or misalignment effects are considered. The backscatter and extinction coefficient profiles at 355, 532, and 1064 nm are computed using the Klett algorithm [*Klett*, 1985], including a synergetic approach with Sun photometer data to select an appropriate lidar ratio (extinction-to-backscatter ratio) value [*Guerrero-Rascado et al.*, 2008]. The lidar ratio is a parameter that depends on many aerosol properties such as chemical composition, size distribution of the particles, and particle shape. The approach consists in computing lidar profiles of extinction coefficient, using different values of lidar ratio as input with 1-sr steps, and the

associated AOD. Thus the AODs obtained by these two methods are compared, and a lidar ratio value is selected when the differences are minimized [*Guerrero-Rascado et al.*, 2008]. According to *Pedrós et al.* [2009], a worst case estimate of the uncertainty associated with the lidar ratio is 10%. After deriving the backscatter coefficient profiles using the appropriate lidar ratio, we compute other properties such as the backscatter-related Ångström exponent profiles. We estimate error bars that consider the effect of the signal-induced noise in the final retrieval using Monte Carlo techniques as established in EARLINET network [*Pappalardo et al.*, 2004; *Guerrero-Rascado et al.*, 2008]. Section 4 deals with the comparison of the profiles of aerosol optical properties retrieved with the lidar system and those determined by means of the airborne PCASP-100X probe.

3.3. Cimel CE 318–4 Sun Photometer

[21] The AOD is considered to be the simplest and single most representative parameter for determining the aerosol loading present in the atmosphere [*Holben et al.*, 2001]. The AOD derived from Sun photometer data is in principal highly accurate (uncertainty less than 0.01 for wavelengths larger than 440 nm and 0.02 for shorter wavelengths) and robust since it does not require any assumption related to the aerosol properties [*Holben et al.*, 1998]. Therefore we will compare the AODs derived by lidar and aircraft measurements with those retrieved from the Sun photometer in section 4. The AOD is derived from the total optical depth obtained by direct Sun measurements [*Alados-Arboledas et al.*, 2003]. A cloud screening filtering is applied to the data [*Smirnov et al.*, 2000]. The Ångström wavelength exponent is a measure of the wavelength dependence of AOD and therefore is sensitive to particle size distribution [*Shifrin*, 1995]. The wavelength exponent can be computed from AOD data.

[22] The sky radiance measurements in the almucantar plane at 440, 670, 870, and 1020 nm in conjunction with solar direct irradiance measurements at these same wavelengths are used to retrieve columnar properties as the volume size distribution, the single scattering albedo (SSA), and the asymmetry parameter at these four wavelengths based on the method of *Nakajima et al.* [1996] using the nonspherical approach proposed by *Olmo et al.* [2006]. In this method, the refractive index is invariant with wavelength. These columnar microphysical properties are derived by iteration, minimizing the residuals between measured and calculated radiances [*Kim et al.*, 2004; *Olmo et al.*, 2006]. The real part of the complex aerosol refractive index used in the iterative process is varied in the range 1.33–1.55 by 0.02 steps, while the imaginary part is set to zero. Then the optimal real part of refractive index obtained by the iterative process is fixed and imaginary part is varied in the range 0–0.01 by 0.0005 steps. The solution of the iterative process gives the columnar size distribution, SSA, asymmetry parameter and optimal refractive index for which the residuals between measured and calculated radiances are minimal.

3.4. Integrating Nephelometer and Multiangle Absorption Photometer

[23] Aerosol scattering and backscattering coefficients were measured with an integrating nephelometer (TSI, model 3563) at three wavelengths 450, 550, and 700 nm. The averaging time was set to 5 min. The zero signal was measured hourly. Owing to nephelometer design limitations, measurements do not cover the full (0°–180°) angular range, and scattering data need correction [e.g., *Anderson and Ogren*, 1998; *Quirantes et al.*, 2008]. In this study, non-idealities due to truncation errors were corrected using the method described by *Anderson and Ogren* [1998] that account for the particle size dependence of the truncation error through the measured wavelength dependence of light scattering. The scattering coefficient shows a minimum dependence on relative humidity (RH) below 50% RH while a sharp increase is evident with RH above 80% [*Anderson and Ogren*, 1998; *Xu et al.*, 2002]. Therefore even if the particles are not chemically dry at RH < 50%, they can be considered dry from a scattering point of view [*Targino et al.*, 2005]. During the study period the RH measured within the nephelometer chamber was below 50%. As a result, the light scattering measurements presented in this study can be considered as dry.

[24] The aerosol light absorption coefficient at 670 nm was recorded with a MAAP. The two reflectivity measurements performed by the system allow for the correction of multiple scattering processes involving the deposited particles and the filter matrix. A detailed description of the method is given by *Petzold and Schönlinner* [2004]. The MAAP draws the ambient air at constant flow rate of 1000 l h^{-1} and operates at a wavelength of 670 nm. The combination of nephelometer and MAAP information provides the SSA at 670 nm.

4. Results and Discussion

4.1. Description of the Synoptical Conditions

[25] Atmospheric processes on regional and local scale play an important role in the variability of aerosol optical properties, especially when the local anthropogenic emissions are considerably reduced. For the El Arenosillo station, natural contributions, such as sea spray and mineral dust, and anthropogenic medium- and long-range transport can be monitored. The atmospheric dynamics and sources of atmospheric aerosol prevailing at the El Arenosillo site, as well as the conditions during the field campaign in 2006 have been described in detail by *Pey et al.* [2008]. Hence only some information on 29 June will be given here.

[26] During the flight day, meteorological conditions were similar to the rest of the days of the campaign (summer sunny day with minimum temperature around 15°C at night and maximum of 28°C at noon). The synoptic scenario, with small pressure gradients over the region, favored that local circulations were controlled by the wind regime of sea-to-land breeze at daytime and land-to-sea breeze at nighttime. These observations are typical at El Arenosillo region [*Adame*, 2005]. It is expected that marine aerosol particles were advected over the study site, at least within the boundary layer during the morning when the INTA-C212 aircraft was airborne. To investigate the aerosol type over El Arenosillo station, the following tools have been used. A 3-day HYSPLIT (http://www.arl.noaa.gov/ready/hysplit4.html) backward trajectory analysis showed that during the campaign air masses were advected from the North Atlantic, overpassed the western Iberian Peninsula and finally reached El Arenosillo station from the ocean. The backward trajectory analysis using a 1° × 1° cell centered on El Arenosillo station (i.e., the backward trajectories ending over the four corners of a cell

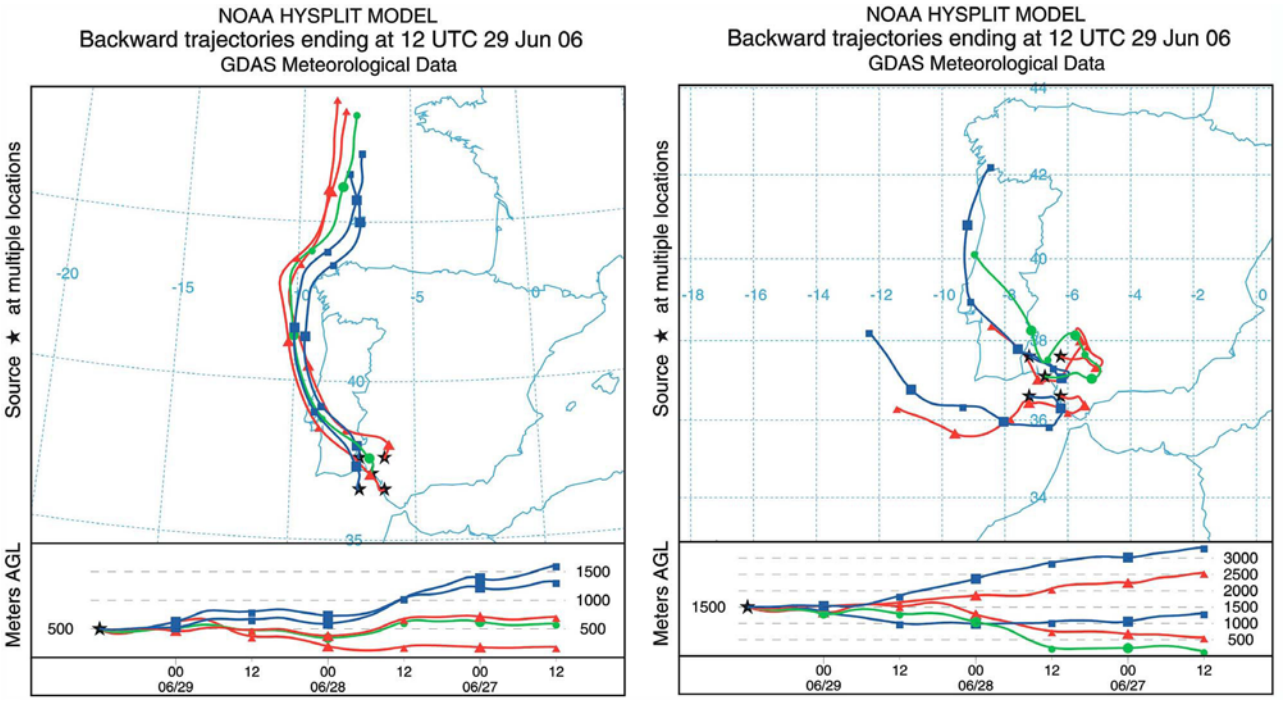

Figure 2. Cells of 3-day backtrajectories ending over El Arenosillo station at 500 and 1500 m (a.s.l.) on 29 June 2006.

centered at the study site) corroborated these backward trajectories (Figure 2). This kind of trajectories corresponds to airflows that are able to advect simultaneously different types of aerosols. Thus in addition to sea spray (as a consequence of sea-to-land breeze), pollutants originated in western cities such as Lisbon, Huelva, and Cadiz, or biomass burning aerosols typical during summer in the south of Iberian Peninsula can be present in the period analyzed. To assess these last contributions, we used the NAAPS model (http://www.nrlmry.navy.mil/aerosol/#currentaerosolmodeling) and MODIS fires data (http://maps.geog.umd.edu/alerts), respectively. NAAPS simulations predicted a low concentration of sulfates (1–2 mg/m^3) at 1200 UTC on 29 June due to the most western flank of a pollution episode that affected almost whole Europe. Moreover, concentrations of smoke particles of 2–4 mg/m^3 were forecasted in the southwestern Iberian Peninsula as an effect of some fires located in this area that took place during the previous day.

[27] In order to confirm the aforementioned description, Sun-photometric and ground-based in situ data have been investigated. Figure 3 shows the evolution of AOD at different wavelengths together with Ångström exponent in several ranges. Several features are observed in this plot. First, data show steadiness along the day, especially in the

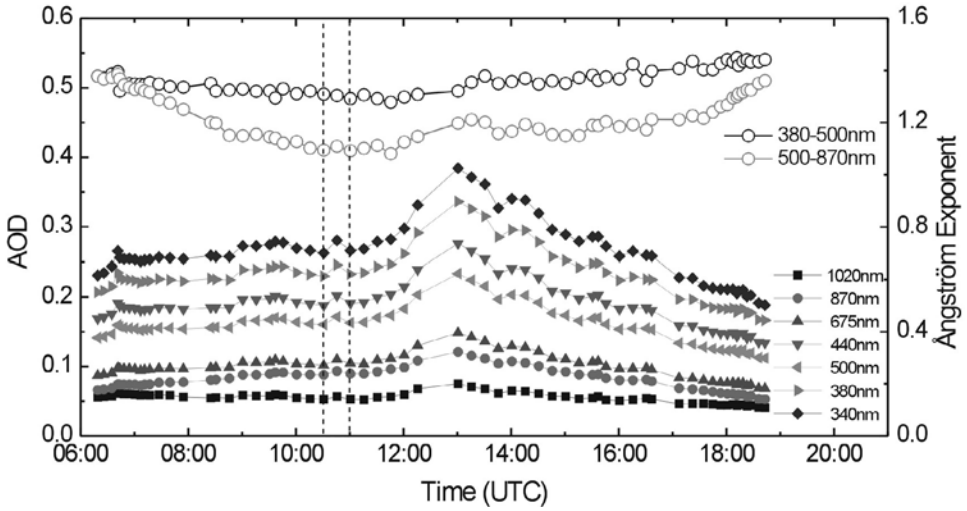

Figure 3. Time series of AOD and Ångström exponents derived by Cimel CE-318 on 29 June 2006. The box focuses on the period when the INTA-C212 aircraft flew close to the station.

Table 2. Typical Parameter of Marine Aerosol Particles Used to Compute Aerosol Optical Properties

Parameter	Value	Reference
m	$1.5 + 10^{-8}$i (355 nm) $1.5 + 10^{-8}$i (532 nm) $1.49 + 2 \cdot 10^{-4}$i (1064 nm)	*Chamaillard et al.* [2003]
c	1.08	*Niedermeier et al.* [2008]
r	2.2 g/cm^3	*Hinds* [1999] *McNaughton et al.* [2007]

morning, with a maximum of AOD for all wavelengths around 1300 UTC. Ångström exponent also exhibits this stability except early in the morning and at the end of the day. Second, the values monitored indicate low aerosol load (AODs lower than 0.15 for $\lambda \geq 675$ nm in the morning) and moderate values of Ångström exponent (1.1–1.4). During the INTA-C212 aircraft flight, AOD was 0.20 and 0.11 at 440 and 675 nm, respectively, and Angström exponent was 1.3 and 1.1 in the range 380–500 and 500–870 nm, respectively. Furthermore, the complex refractive index derived from Cimel at 0932 UTC is 1.49+0.008i and the SSA is 0.90 at 670 nm. Previous studies at this site [i.e., *Toledano et al.*, 2007] provided information about aerosol type on the basis of Cimel-derived computations and selection criteria were established. For this 5-year climatology, marine particles presented AODs at 440 nm below 0.2 with Ångström exponent between 0 and 2. In addition, the authors found that the absorbing aerosols as continental and biomass burning particles showed Ångström exponents larger than 1.05 and 1.4, respectively, with AOD larger than 0.2.

[28] The SSA at surface computed by the combination of nephelometer and MAAP was 0.91 at 670 nm with a standard deviation of 0.01 during the flight. This value supports our hypothesis of polluted marine aerosols. According to *Hess et al.* [1998] and *Smirnov et al.* [2003] clean maritime particles are responsible of AODs at 440 nm smaller than 0.2. *Dubovik et al.* [2002] showed that the oceanic aerosol is characterized at 440 nm by AOD $\leq$ 0.15 and SSA = 0.98 ± 0.03. The smaller SSA values found by *Santese et al.* [2008] (SSA = 0.94 ± 0.03, with minimum and maximum values of 0.90 and 0.98, respectively) respect to the ones reported by *D'Almeida* [1991] and *Dubovik et al.* [2002] for marine aerosol were explained by assuming that fine-mode and moderately absorbing particles of non-marine origin affected the aerosol. In addition, *Omar et al.* [2005] reported AOD and SSA of 0.140 and 0.93, respectively, at 673 nm, for the polluted marine category.

[29] Therefore we can infer that a mixture of marine aerosol with a small signature of absorbing particles was present at El Arenosillo station during the period analyzed, as we initially hypothesized. As a consequence, our computations during the flight have been based on the values in Table 2.

4.2. Vertical Atmospheric Structure During the Flight

[30] Figure 4 presents the temporal evolution of range corrected signal (in arbitrary units) at 532 nm over El Arenosillo station obtained by the lidar system LR321D400 during the morning of 29 June. The development of the boundary layer along the morning can be seen together with some steady layers located in upper levels. The morning is characterized by a marked stability in the whole atmospheric column. Thus the development of the boundary layer only implies changes in the vertical distribution of aerosol particles, whereas the optical properties such as the AOD remain practically unchanged, as Figure 3 shows. The box in Figure 4 focuses on the period 1030–1100 UTC, when the INTA-C212 plane flew over the station. In this period the variability of aerosol layering is negligible (the mean value of the variability is 2.7% for the thorough range sounded and less than 3.1% for altitudes below 1 km) and hence, the mean vertical lidar profiles are representative from 1030 to 1100 UTC. In addition, Figure 4 reveals that the largest aerosol load is confined below 1 km, where a marine signature is expected due to the typical wind regime of sea-to-land breeze during daytime. Above it a second layer extends up to 1.7 km approximately, where a sharp decrease of backscattered lidar signal indicates the beginning of the free troposphere.

[31] Figure 5 shows the vertical profiles of temperature, water vapor mixing ratio, logarithmic derivate of range cor-

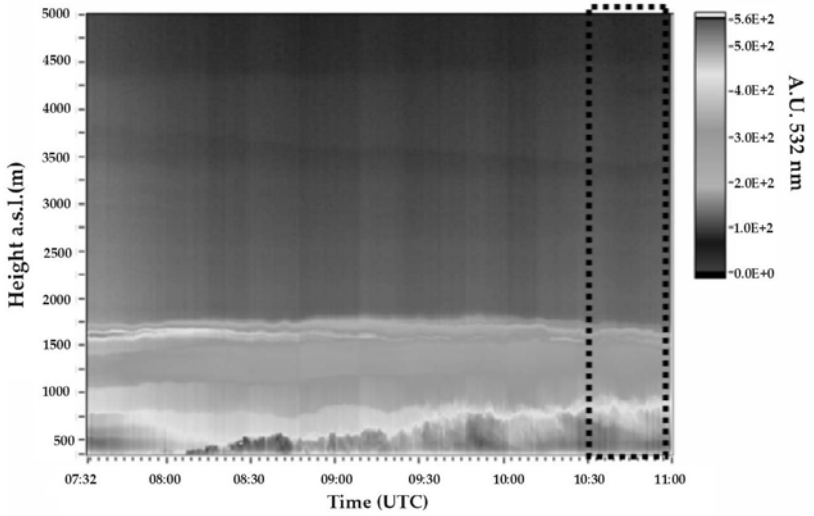

Figure 4. Temporal evolution of range corrected lidar signal at 532 nm during 29 June 2006. The box focuses on the period when the INTA-C212 aircraft flew close to the station.

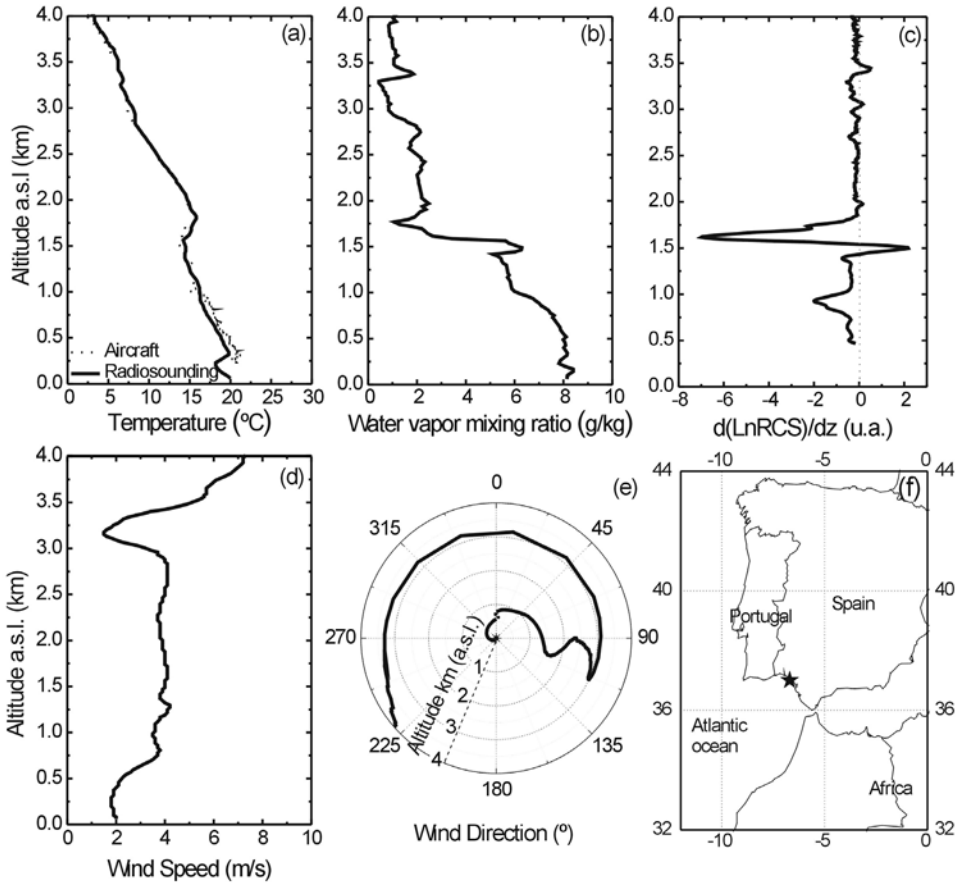

Figure 5. Vertical profiles of (a) temperature, (b) water vapor mixing ratio, (c) logarithmic derivate of range corrected lidar signal at 532 nm, (d) wind speed, (e) wind direction, and (f) reference system centered at El Arenosillo station. Radiosounding was launched at 1102 UTC, aircraft data were measured between 1027 and 1044 UTC, and lidar profile was obtained between 1030 and 1100 UTC.

rected signal, wind speed, and wind direction profiles on 29 June. Several layers are present over El Arenosillo, as it can be seen in the temperature profile (Figure 5a). Two temperature inversions are detected at around 300 m and 1600 m. At that last altitude the aerosols observed in Figure 4 are capped by the upper temperature inversion. A peak in water vapor mixing ratio (Figure 5b) occurs at the top of this layer, associated to the bottom of this inversion. Water vapor mixing ratio remains below 2.5 g/kg in the free troposphere region and between 5.0 and 8.5 g/kg in the surface layers containing aerosols. The analysis of the logarithmic derivate of the range corrected signal is in agreement with the thermal structure: it reveals a boundary layer at 930 m and a top layer up to 1620 m. The uncertainty of the logarithmic gradient method determined by Monte Carlo techniques is ±15 m and arises from the numerical procedure to compute the derivate (linear fit) and the sliding window for fitting and smoothing (three points). As will be shown below, there are no significant differences in aerosol optical and microphysical intensive properties between layers below and above 930 m (excluding the free troposphere region). Thus we denoted the layer from surface up to 930 m as layer 1, and the layer from this altitude up to 1620 m corresponds to the layer 2.

[32] The top of the layer 1 is found at 930 m according to the lidar profile. It is in agreement with thermodynamic techniques, such as the Richardson number method, which is based on the combination of profiles of wind speed and potential temperature to determine the top of the boundary layer [*Sicard et al.*, 2006]. For this case, the Richardson number method gives a top height at 1035 m. The different nature of both methods explains the discrepancy observed. Moreover, the temperature profile (Figure 5a) reveals an isothermal layer at 910–1090 m (with a temperature around 16°C), a range that includes the altitudes of the top of layer 1 obtained by both methods.

4.3. Volume Size Distributions

[33] Size distributions have been routinely retrieved by inversion of clear sky almucantar scans of radiance as a function of scattering angle by the Cimel Sun photometer. The Cimel Sun photometer distributions are derived from the measured solar direct irradiances and sky radiances, and they represent a columnar-averaged size distribution. In contrast, the aircraft measurements are able to produce a profile of size distributions. Therefore in order to compare both set of measurements, the aircraft data have been transformed to a column mean distribution averaged over the whole range sounded by the aircraft. In addition, for comparison, size distributions have been normalized by dividing by the max-

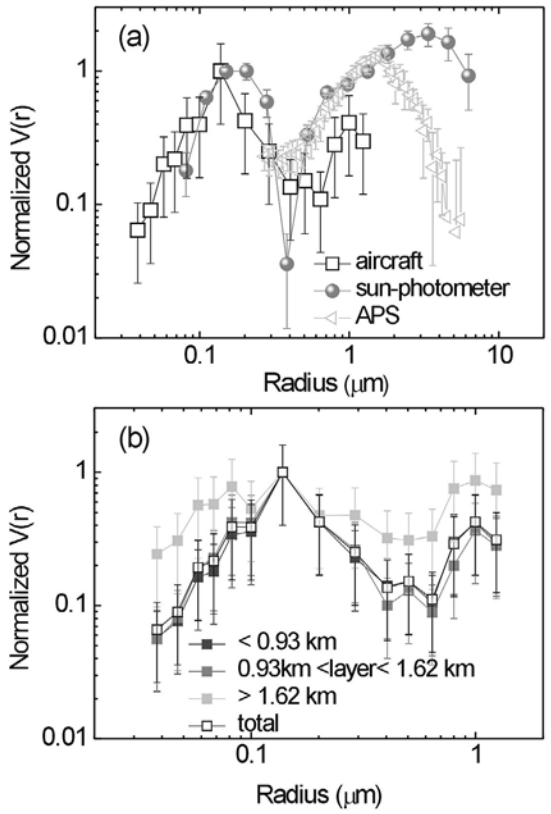

Figure 6. Normalized aerosol volume size distributions (a) inverted from aircraft data (averaged over the range sounded), Sun photometer sky radiance (whole column integrated), and APS (at ground level); (b) inverted from aircraft data over the different layers detected on 29 June 2006. Errors bars are correspond to the propagations of errors for the aircraft data and for the Cimel Sun photometer is the standard deviation computed over the size distributions retrieved.

imum in the distribution, corresponding to the fine mode peak for both data sets.

[34] Figure 6a shows the normalized size distributions derived by Cimel Sun photometer (whole column integrated) and by aircraft data (averaged over the range (0.25–4.1 km)). The comparison is reasonable within uncertainty, although with some differences both in fine and coarse mode. A slight displacement of aerosol volume to the fine mode can be observed in the aircraft data and the plot suggests the agreement is better in the fine mode with obvious discrepancies in the coarse mode (>1 mm). The mean absolutes differences for the normalized size distributions are 0.19 and 0.43 (in arbitrary units) for radii below and above 0.5 mm, respectively. For comparison, Figure 6a also includes the normalized size distribution derived by APS at ground level (because of the absence of the fine mode in the APS data the normalization was performed respect to the coarse mode of the Cimel Sun photometer). The comparison is quite reasonable within uncertainty especially for radii up to 2 mm. It must be taken into account that here we compare volume size distributions retrieved from optical measurements (Sun photometer and PCASP sonde) and those obtained by classifications in different aerodynamic radii bins (APS).

[35] This comparison is limited by several experimental conditions. First, the measurement time of the aircraft (around 1027 UTC), the Sun photometer (0932 UTC), and the APS (1030–1100 UTC) differs. Second, these size distributions are biased due to the range covered for each instrument. The range investigated with aircraft data is 0.1 to 3.0 mm in diameter, whereas the range for Sun-photometric data is 0.05 to 10 mm. This imply a biased toward low radius in the aircraft retrievals with respect to the Sun-photometric ones. As shown by *Collins et al.* [2000], the size bin threshold settings are particularly sensitive to the imaginary part of the refractive index, and hence neglecting absorption causes particles (particularly supermicron) to be undersized. Moreover, humidity modifies the size of particles and so any drying of the sample within the PCASP will make the particles smaller than in the ambient atmospheric state. Finally, an additional error source must be taken into account in this comparison regarding to the representativeness of the size distributions in the range sounded by the aircraft. The Cimel Sun photometer retrieval provides information of the whole atmospheric column, whereas the aircraft data are limited to the range (0.25–4.1 km).

[36] We have performed inversions for each detected layer to study the influence of the multiple aerosol layers in the retrieval of our columnar size distributions. Figure 6b presents the normalized volume size distributions retrieved for layer 1 (0.25–0.93 km), layer 2 (0.93–1.62 km), free troposphere (1.62–4.1 km), and the total range sounded (0.25–4.1 km), where the layer heights have been determined from the lidar profile. As it can be seen from the plot, the volume size distributions are coincident in the layers 1 and 2, indicating that particles included in both layers exhibit the same features. Moreover, the retrieval for the total range is coincident with the inversions in both layers (with mean differences around 10%) and, therefore the effect of the free troposphere is minimal for the total averaging.

4.4. Extinction Profiles and Aerosol Optical Depth

[37] Profiles of backscatter coefficients at 355, 532, and 1064 nm derived from aircraft data and lidar analyses have been compared (not shown here). The aircraft in situ measurements and lidar agree on magnitude and vertical gradient of aerosol extinction coefficient and also on the height of different layers (differences less than 10% and 2% for the top of layers 1 and 2, respectively) (Figure 7). The differences that are found may have been partly caused by the inhomogeneity in the aerosol distribution in the atmosphere. Similar differences have been detected in other comparisons of in situ measurements on board aircraft and lidar and were attributed to differences in the timing and location of profiles in inhomogeneous aerosol field [*Schmid et al.*, 2006; *Osborne et al.*, 2007]. In any case, a typical feature is that profiles derived by airborne measurements showed a signal-to-noise ratio lower than that derived by lidar (Figure 7).

[38] Similar aerosol layering is found in both airborne and lidar extinction measurements. In general, the presence of aerosol particles was detected up to 1.7 km (a.s.l.). The largest values of extinction coefficient were found between the ground up to approximately 1 km (a.s.l.) and are mainly due to marine particles in the layer 1. Above this layer and up to 1.7 km, relative high values are also observed. Extinction

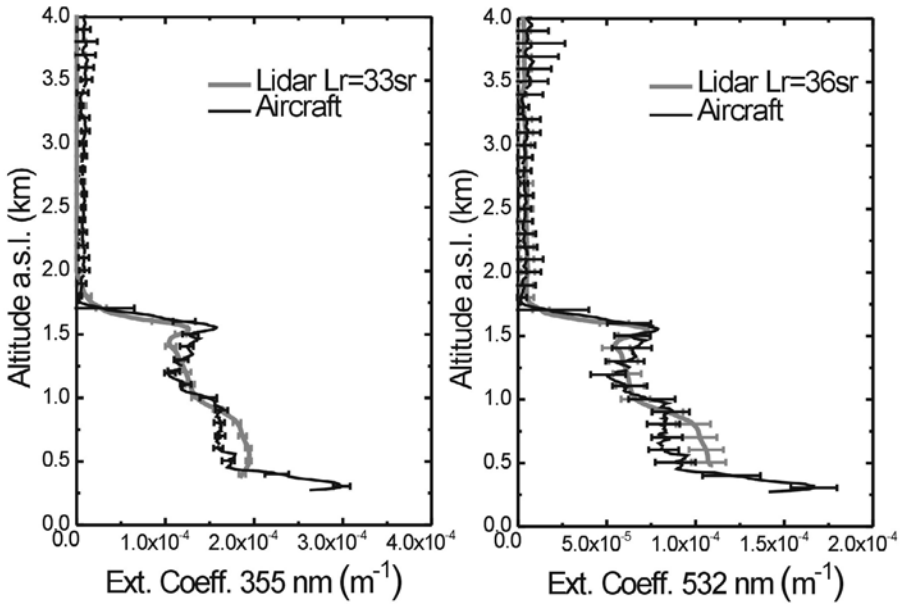

Figure 7. Extinction coefficient profiles at 355 and 532 nm derived by lidar and aircraft in situ instrumentation on 29 June 2006. Error bars for lidar retrievals have been computed using Monte Carlo techniques and for aircraft data are an estimation of 20%. Plots include the lidar ratio used to derive extinction coefficient profiles by Klett algorithm.

coefficients derived by both instruments decrease drastically above 1.7 km, indicating the absence of aerosol particles in the free troposphere.

[39] We have also analyzed the relative differences in aerosol extinction coefficient profiles obtained by lidar and PCASP during the flight. The relative differences are less than 20% at 355 and 532nm (Figure 7), and less than 30% at 1064 nm (not shown here), in the region with high aerosol concentration. These values are exceeded in the region where the temperature inversion (around 1.6 km) was detected by the aircraft temperature sensors (Figure 5).

[40] Aircraft in situ and lidar measurements have uncertainties associated with aerosol physical and optical properties and also with different inversion methodologies. Therefore it is important to assess the measurements against a direct and more reliable measurement of aerosol in the atmospheric column. For this work, we can consider that the measurement of AOD derived by Sun photometer is the most accurate and robust because it does not require any assumption related to aerosol properties. Therefore we will compare the AODs derived by lidar and aircraft measurements with those retrieved from the Sun photometer. The measurement derived by Sun photometer provided values of 0.26, 0.16, and 0.05 at 355, 532, and 1064 nm, respectively, coincident with the time of flight. To perform this comparison, it must be taken into account the range of altitudes sounded by each technique. For the aircraft computations the data acquisition started at 230 m above ground level, and the lidar technique provides aerosol optical properties profiles above the full overlap altitude. This altitude is defined as the altitude in which the laser beam is fully included in the field of view of the receiver telescope. The AODs computed in the height ranges covered by lidar and aircraft measurements (above 370, 470, and 630 m at 355, 532, and 1064 nm, respectively, for a full overlap), show a good agreement. Absolutes differences are less than 0.01 at 532 and 1064 nm and less than 0.02 at 355 nm. The magnitude of these differences is lower than the uncertainties assumed in the AOD obtained from elastic lidar [*Guerrero-Rascado et al.*, 2008].

[41] Other comparisons of AODs determined by means of aircraft and Sun-photometric data can be found in the literature. The AODs derived by the combination of an integrating nephelometer and PSAP shown good agreement with AERONET Sun photometer for biomass burning [*Haywood et al.*, 2003]. However, AODs determined by PCASP produced low values of extinction coefficient because of a bias in total concentrations of coarse particles as a consequence of the poor measurement capability for particles in this size range [*Haywood et al.*, 2003, *Osborne et al.*, 2007; *Johnson et al.*, 2008]. For the case presented in this study, the aircraft AODs are lower than the Sun photometer values. As it was expected, a poorer agreement between aircraft and Sun photometer AOD is observed in the visible and ultraviolet range. The aircraft AOD at 355 nm (0.24) agrees with the Sun photometer value (0.26) within the uncertainty range (0.02) [*Holben et al.*, 1998]. However, differences larger than the uncertainty (0.12 versus 0.16) are observed at 532 nm. These disagreements are caused fundamentally by the lack of information below 230 m in the aircraft computations.

[42] In addition, we perform the estimation of the fine and coarse contribution to the total AOD at 500 nm from the Sun photometer data and from the combination of aircraft data and APS ground level measurements. Using the Mie code and cutoff radius of 0.5 mm, we obtain a fine fraction (fine AOD to total AOD ratio) of 0.79 and 0.78 for the Sun-photometer and the combination of aircraft plus APS, respectively. The small differences may be minimized accurately measuring the coarse mode with the aircraft.

Table 3. Ångström Exponent at Different Spectral Ranges Derived by In Situ Aircraft Measurements and Lidar During the Flight on 29 June[a]

Altitude (km)	Layer	Ångström Exponent 355–532 (nm)	532–1064 (nm)	380–500 (nm)	500–870 (nm)
		In Situ Aircraft Measurement			
0.25–0.93	1	1.60 ± 0.07	1.48 ± 0.11		
0.93–1.62	2	1.67 ± 0.06	1.61 ± 0.19		
0.25–1.62	effective	1.63 ± 0.07	1.55 ± 0.17		
		Lidar			
0.25–0.93	1	1.50 ± 0.05	1.50 ± 0.04		
0.93–1.62	2	1.63 ± 0.13	1.80 ± 0.14		
0.25–1.62	effective	1.57 ± 0.12	1.71 ± 0.18		
		Cimel			
All columns	effective			1.3 ± 0.2	1.1 ± 0.2

[a]Cimel Sun photometer Ångström exponent is also included. The term "effective" includes the layers 1 and 2 for the lidar and the aircraft computations and the whole atmospheric column for Cimel data.

4.5. Ångström Exponent

[43] Table 3 shows the comparison between sun-photometric Ångström exponents and those computed over aerosol extinction profiles derived by lidar and in situ aircraft data. The Ångström exponent derived either by the lidar or the aircraft data for all altitude ranges is above 1.50 in the spectral range 355–532 nm and above 1.48 in the spectral range 532–1064 nm. The differences with the Sun-photometric Ångström exponents have maximum values of 10% in the spectral range of 355–532 nm and around 15% in the spectral ranges 532–1064 nm, although most values are below 5%. There are similarities between Ångström exponents in the layer 1 and 2. This seems to be consistent with the behavior of volume size distributions in both layers, where negligible differences were found (see section 4.4). However, discrepancies become more significant with respect to the Sun-photometric Ångström exponents, which are 1.3 and 1.1 in the spectral range 380–500 and 500–870 nm, respectively. As mentioned previously, it must be taken into account that the Sun-photometric data provide information of the whole atmospheric column, including the lowest part of the boundary layer, which are neither sounded by the aircraft nor by the lidar, and also the free troposphere. Furthermore, an additional discrepancy source arises from the spectral range investigated by both profiler instruments (aircraft and lidar) and Sun photometer.

4.6. Lidar Ratio

[44] In this section we compare lidar ratio values retrieved from elastic lidar signals constrained by Sun-photometric data (section 3.2) with those calculated from in situ aircraft measurements (section 3.1) in several layers. While the aerosol extinction coefficient is sensitive mainly to the aerosol size distribution and the real part of the refractive index, the lidar ratio also depends on the imaginary part, mixing stage (i.e., the relative contribution of internal and/or external aerosol mixing), and shape of the particles because the backscatter coefficient is sensitive to these properties [*Kuzmanoski et al.*, 2007]. Therefore this comparison is convenient for testing the validity of the aerosol model in estimating other aerosol optical properties [*Kuzmanoski et al.*, 2007].

[45] The lidar ratios used to retrieve the profiles of aerosol extinction coefficients from lidar data were selected by an iterative approach based on Sun-photometric data. The lidar ratios derived by in situ aircraft measurements are shown in Table 4. The values derived from aircraft data indicate that the variability between layer 1 (below 0.93 km) and layer 2 (from 0.93 to 1.62 km) is negligible for all wavelengths. This fact was also found for other aerosol properties such as the normalized volume size distribution (section 4.3) and Ångström exponent (section 4.5) and was also expected from the analysis of meteorological parameters (section 4.2). Only some minor differences are detected in the free troposphere as a result of marked differences related to the type of atmospheric component (aerosol particles signature versus molecular signal). In this region, the signal-to-noise ratio of the lidar ratio profiles decreases considerably, and thus the standard deviation for this layer increases dramatically.

[46] The lidar ratios used to retrieve optical properties from the lidar system were 33, 36, and 26 sr at 355, 532, and 1064 nm, respectively, as shown in Figure 7 and Table 4. These columnar values reveal some discrepancies with respect to the in situ aircraft measurements. We must keep in mind that these are effective values for the whole atmospheric column, and thus they correspond to a weighted average of lidar ratios representative of different layers, among them the lowest one not sounded by the aircraft (below 250 m) and the free troposphere. We consider that these disagreements of around 20% are caused fundamentally by the different type of scatterers and absorbers in the region sounded by the aircraft respect to those in the lowest troposphere.

[47] The values derived by in situ aircraft measurements and obtained by combination of lidar and Sun-photometric data agree with typical lidar ratios for marine particles

Table 4. Lidar Ratios at Different Wavelengths Derived by In Situ Aircraft Measurements and by Combination of Lidar and Cimel Sun Photometer Combination During the Flight on 29 June

Altitude (km)	Layer	Lidar Ratio (sr) 355 (nm)	532 (nm)	1064 (nm)
		In Situ Aircraft Measurement		
0.25–0.93	1	39 ± 1	31 ± 2	24 ± 3
0.93–1.62	2	40 ± 2	32 ± 3	22 ± 3
1.62–4.10	FT	31 ± 6	27 ± 7	35 ± 12
All column	effective	34 ± 6	28 ± 6	31 ± 11
		Lidar-Cimel Combination		
All column	effective	33 ± 3	36 ± 4	26 ± 3

Table 5. Lidar Ratios Observed Under Maritime Conditions in Different Locations

Instrument	Place	Observations	Lidar Ratio (sr)			Reference
			355 (nm)	532 (nm)	1064 (nm)	
Raman lidar	North Atlantic	ACE2	-	23 ± 3	-	*Müller et al.* [2007]
Raman lidar	Tropical Indian Ocean	INDOEX	-	23 ± 5 (PBL) 29 ± 8 (FT)	-	*Müller et al.* [2007]
Raman lidar	South Italy	EARLINET	-	23–44[a]	-	*De Tomasi and Perrone* [2003]
Raman lidar	Greece	EARLINET	28 ± 11	-	-	*Amiridis et al.* [2005]
-	-	Numerical study	15–30	15–30	25–50	*Ackermann* [1998]
Sun photometer	26 stations	AERONET sites	-	28 ± 5[b]	-	*Cattrall et al.* [2005]
Micropulsed lidar + Sun photometer	Tropical Indian Ocean	INDOEX	-	33 ± 6	-	*Welton et al.* [2002]
Nephelometer + PSAP		clean marine conditions	-	25.4 ± 3.5	-	*Masonis et al.* [2003]

[a]Lidar ratio at 531 nm.
[b]Lidar ratio at 550 nm.

reported by other authors. Some examples of lidar ratios obtained using several instruments in different locations under maritime conditions are shown in Table 5. We can conclude that the lidar ratio values obtained in this study support the marine nature of the aerosol particles present during the measurements. Moreover, our analysis (section 4.1) evidences a small signature of absorbing particles as it was indicated by the in situ SSA (0.91 ± 0.01). This increase in the extinction contribution leads to an increase of the lidar ratio when compare with that typical of background marine conditions.

5. Conclusions

[48] The studies of aerosol particles require the use of different instrumentation and methodologies to properly characterize them. As a consequence, the agreement among parameters derived from diverse devices and procedures must be checked. The comparison of the major optical and microphysical properties of aerosol particles derived from both aircraft and ground based remote sensing were the subject of this paper.

[49] The closure experiment on aerosol measurements (lidar, airborne, and Sun photometer) over El Arenosillo station during DAMOCLES field campaign on 29 June has shown that within experimental uncertainty, there is consistency between the collected data. The aerosol loading was contained within two distinguishable layers: layer 1 between the surface and 930 m and layer 2 from 930 m to 1620 m. The volume size distributions indicated that particles inside both layers exhibit the same microphysical features, in terms of volume size distributions (with mean differences around 10%). A slight displacement of aerosol volume to the fine mode can be observed in the aircraft data respect to the columnar size distribution retrieved by Sun photometer caused by different timing, the bias related to the range covered for each instrument, and the representativeness of the aircraft data in the range sounded of the whole atmospheric column (including the lowest part of the troposphere).

[50] The aircraft measurements and lidar concur both on magnitude and vertical gradient of the aerosol extinction coefficient and also on the height of different layers. The relative differences were less than 20% at 355 and 532 nm and less than 30% at 1064 nm, in the region with high aerosol concentration. These differences may have been partly caused by differences in sampling of extensive properties in nonuniform spatial distribution of the aerosol. The AOD computed in the height ranges covered by lidar and aircraft measurements displayed a good agreement with absolute differences less than the uncertainties of the lidar inversion method. The computation of associated Ångström exponents using both techniques also agreed, with maximum differences of 10% in the range 355–532 nm and around 15% in the range 532–1064 nm, respectively, although values below 5% were found for almost the whole range sounded.

[51] The lidar ratios for all wavelengths derived by aircraft indicate that the variability between layers 1 and 2 was negligible. This vertical homogeneity was also found for other aerosol properties as normalized volume size distribution and the Ångström exponent and was expected from the analysis of meteorological parameters.

[52] Acknowledgments. This work has been supported by Spanish Ministry of Education and Science under the Acciones Complementarias CGL-2006-27108-E/CLI (DAMOCLES Aerosol Scientific Thematic Network), and CGL2008-01330-E/CLI (Spanish and Portuguese Aerosol Lidar Network) and CGL2009-08031-E/CLI (Participación española en ChArMEx); project CGL2007-66477-C02-01, CSD2007-00067, CGL2004-05984-C07-03, CGL2007-60648 and CGL2009-07790 of the Spanish Ministry of Education; project P08-RNM-3568 and P06-RNM-01503 of the Autonomous Government of Andalusia; and by the EARLINET-ASOS project (EU Coordination Action, contract 025991 (RICA)). We are indebted to the staff at INTA-Arenosillo for the technical support during the campaign. The authors are grateful to Spanish Air Force and C-212 crew for their interest and support during the campaign and also to the HYSPLIT transport and dispersion model. We are in debt to the two anonymous reviewers that have contributed to improve the quality of the paper with their comments and suggestions.

References

Ackerman, S., O. B. Toon, D. E. Stevens, A. J. Heymsfield, V. Ramanathan, and E. J. Welton (2000), Reduction of tropical cloudiness, *Science*, *288*, 1042–1047, doi:10.1126/science.288.5468.1042.

Ackermann, J. (1998), The extinction-to-backscatter ratio of tropospheric aerosol: A numerical study, *J. Atmos. Oceanic Technol.*, *15*, 1043–1050, doi:10.1175/1520-0426(1998)015<1043:TETBRO>2.0.CO;2.

Adame, J. A. (2005), Caracterización y comportamiento del ozono superficial en la provincia de Huelva, Ph.D. thesis, Univ. de Huelva, Huelva, Spain.

Alados-Arboledas, L., H. Lyamani, and F. J. Olmo (2003), Aerosol size properties at Armilla, Granada (Spain), *Q. J. R. Meteorol. Soc.*, *129*(590), 1395–1413, doi:10.1256/qj.01.207.

Alados-Arboledas, L., et al. (2004), Veleta 2002 field campaign a general overview, *Opt. Pura Apl.*, *37*(3), 3271–3276.

Alados-Arboledas, L., et al. (2008), Aerosol columnar properties retrieved from CIMEL radiometers during VELETA 2002, *Atmos. Environ.*, *42*, 2654–2667, doi:10.1016/j.atmosenv.2007.10.006.

Alcántar-Ruiz, A., F. J. Olmo, and L. Alados-Arboledas (2004), Langley calibrations of sunphotometer at Sierra Nevada, Granada, Spain, *Opt. Pura Apl.*, *37*, 3263–3269.

Amiridis, V., D. S. Balis, S. Kazidzis, A. Bais, and E. Giannakaki (2005), Four-year aerosol observation with a Raman Lidar at Thessaloniki, Greece, in the framework of the European Aerosol Research Lidar Network (EARLINET), *J. Geophys. Res.*, *110*, D21203, doi:10.1029/2005JD006190.

Anderson, T. L., and J. A. Ogren (1998), Determining aerosol radiative properties using the TSI 3563 integrating nephelometer, *Aerosol Sci. Technol.*, *29*, 57–69, doi:10.1080/02786829808965551.

Baumgardner, D., and M. Spowart (1990), Evaluation of the forward scattering spectrometer probe: Part III. Time response and laser inhomogeneity limitations, *J. Atmos. Oceanic Technol.*, *7*, 666–672, doi:10.1175/1520-0426(1990)007<0666:EOTFSS>2.0.CO;2.

Baumgardner, D., W. Srapp, and J. E. Dye (1985), Evaluation of the forward scattering spectrometer probe. Part II: Corrections for coincidence and dead-time losses, *J. Atmos. Oceanic Technol.*, *2*, 626–632, doi:10.1175/1520-0426(1985)002<0626:EOTFSS>2.0.CO;2.

Baumgardner, D., J. E. Dye, R. G. Knollenberg, and B. W. Gandrud (1992), Interpretation of measurements made by the FSSP-300X during the Airborne Arctic Stratospheric Expedition, *J. Geophys. Res.*, *97*, 8035–8046.

Baumgardner, D., G. B. Raga, J. C. Jimenez, and K. Bower (2005), Aerosol particles in the Mexican East Pacific Part I: Processing and vertical redistribution by clouds, *Atmos. Chem. Phys.*, *5*, 3081–3091, doi:10.5194/acp-5-3081-2005.

Binnig, J., J. Meyer, and G. Kasper (2007), Calibration of an optical particle counter to provide PM2.5 mass for well-defined particle materials, *J. Aerosol Sci.*, *38*, 325–332, doi:10.1016/j.jaerosci.2006.12.001.

Bohren, C. F., and D. R. Huffman (1983), *Absorption and Scattering of Light by Small Part*, John Wiley, Hoboken, N. J.

Bösenberg, J., et al. (2001), EARLINET: A European aerosol research lidar network, in *Laser Remote Sensing of the Atmosphere*, edited by A. Dabas, C. Loth, and J. Pelon, pp. 155–158, Ecole Polytech., Palaiseau, France.

Cattrall, C., J. Reagan, K. Thome, and O. Dubovik (2005), Variability of aerosol and spectral lidar and backscatter and extinction ratios of key aerosol types derived from selected Aerosol Robotic Network locations, *J. Geophys. Res.*, *110*, D10S11, doi:10.1029/2004JD005124.

Chamaillard, K., S. G. Jennings, C. Kleefeld, D. Ceburnis, and Y. J. Yoon (2003), Light backscattering and scattering by nonspherical sea-salt aerosols, *J. Quant. Spectrosc. Radiat. Transfer*, *79–80*, 577–597.

Collins, D. R., et al. (2000), In situ aerosol size distributions and clear column radiative closure during ACE2, *Tellus, Ser. B*, *52*, 498–525, doi:10.1034/j.1600-0889.2000.00008.x.

D'Almeida, G. A. (1991), *Atmospheric Aerosols: Global Climatology and Radiative Characteristics*, A. Deepak, Hampton, Va.

De Tomasi, F., and M. R. Perrone (2003), Lidar measurements of tropospheric water vapour and aerosol profiles over southeastern Italy, *J. Geophys. Res.*, *108*(D9), 4286, doi:10.1029/2002JD002781.

Dubovik, O., B. N. Holben, T. Lapyonok, A. Sinyk, M. I. Mishechenko, P. Yang, and I. Slutsker (2002), Non-spherical aerosol retrieval method employing light scattering by spheroids, *Geophys. Res. Lett.*, *29*(10), 1415, doi:10.1029/2001GL014506.

Estellés, V., A. Esteve, J. Pey, J. A. Martinez-Lozano, M. P. Utrillas, X. Querol, J. de la Rosa, Y. Gonzalez-Castanedo, A. Alastuey, and G. Gangoiti (2009), Preliminary analysis of columnar aerosol properties in relation to surface PM measurements in the DAMOCLES 2006 field campaign (Spain), *Geophys. Res. Abstr.*, *11*, EGU2009-10988-1.

Fiebig, M., A. Petzold, U. Wandinger, M. Wendisch, C. Kiemle, A. Stifter, M. Ebert, T. Rother, and U. Leiterer (2002), Optical closure for an aerosol column: Method, accuracy, and inferable properties applied to a biomass-burning aerosol and its radiative forcing, *J. Geophys. Res.*, *107*(D21), 8130, doi:10.1029/2000JD000192.

Gadhavi, H., and A. Jayaraman (2006), Airborne lidar study of the vertical distribution of aerosol over Hyderabad, an urban site in central India, and its implication for radiative forcing calculations, *Ann. Geophys.*, *24*(10), 2461–2470, doi:10.5194/angeo-24-2461-2006.

Guerrero-Rascado, J. L., B. Ruiz, and L. Alados-Arboledas (2008), Multi-spectral lidar characterization of the vertical structure of Saharan dust aerosol over southern Spain, *Atmos. Environ.*, *42*, 2668–2681, doi:10.1016/j.atmosenv.2007.12.062.

Haywood, J. M., and V. Ramaswamy (1998), Global sensitivity studies of the direct radiative forcing due to anthropogenic sulfate and black carbon aerosols, *J. Geophys. Res.*, *103*(D6), 6043–6058, doi:10.1029/97JD03426.

Haywood, J., P. Francis, O. Dubovik, M. Glew, and B. Holben (2003), Comparison of aerosol size distributions, radiative properties, and optical depths determined by aircraft observations and Sun photometers during SAFARI 2000, *J. Geophys. Res.*, *108*(D13), 8471, doi:10.1029/2002JD002250.

Hess, M., P. Koepke, and I. Schult (1998), Optical properties of aerosols and clouds: The software package OPAC, *Bull. Am. Meteorol. Soc.*, *79*, 831–844, doi:10.1175/1520-0477(1998)079<0831:OPOAAC>2.0.CO;2.

Hinds, W. C. (1999), *Aerosols Technology: Properties, Behavior and Measurement of Airborne Particles*, 2nd ed., John Wiley, New York.

Holben, B. N., et al. (1998), Aeronet—A federated instrument network and data archive for aerosol characterization, *Remote Sens. Environ.*, *66*, 1–16, doi:10.1016/S0034-4257(98)00031-5.

Holben, B. N., et al. (2001), An emerging ground-based aerosol climatology: Aerosol optical depth from AERONET, *J. Geophys. Res.*, *106*(D11), 12,067–12,097.

Johnson, B. T., S. R. Osborne, J. M. Haywood, and M. Harrison (2008), Aircraft measurements of biomass burning aerosol over West Africa during DABEX, *J. Geophys. Res.*, *113*, D00C06, doi:10.1029/2007JD009451.

Kim, D. H., B. J. Sohn, T. Nakajima, T. Takamura, T. Takemura, B. C. Choi, and S. C. Yoon (2004), Aerosol optical properties over East Asia determined from ground-based sky radiation measurements, *J. Geophys. Res.*, *109*, D02209, doi:10.1029/2003JD003387.

Kim, Y. J., and J. F. Boatman (1990), Size calibration corrections for the Active Scattering Aerosol Spectrometer Probe (ASASP-100X), *Aerosol Sci. Technol.*, *12*, 665–672, doi:10.1080/02786829008959381.

Klett, J. D. (1985), Lidar inversion with variable backscatter/extinction ratios, *Appl. Opt.*, *24*, 1638–1643, doi:10.1364/AO.24.001638.

Kuzmanoski, M., M. A. Box, B. Schmid, G. P. Box, J. Wang, P. B. Russell, D. Bates, H. H. Jonsson, E. J. Welton, and J. H. Seinfeld (2007), Aerosol properties computed from aircraft-based observations during the ACE-Asia campaign: 2. A case study of Lidar ratio closure, *Aerosol Sci. Technol.*, *41*, 231–243, doi:10.1080/02786820601146977.

Masonis, S. J., T. L. Anderson, D. S. Covert, V. Kapustin, A. D. Clarke, S. Howell, and K. Moore (2003), A study of the extinction-to-backscatter ratio of marine aerosol during the Shoreline Environment Aerosol Study, *J. Atmos. Oceanic Technol.*, *20*, 1388–1402, doi:10.1175/1520-0426(2003)020<1388:ASOTER>2.0.CO;2.

McFarquhar, G. M., and H. L. Wang (2006), Effects of aerosols on trade wind cumuli over the Indian Ocean: Model simulations, *Q. J. R. Meteorol. Soc.*, *132*, 821–843, doi:10.1256/qj.04.179.

McNaughton, C. S., et al. (2007), Results from the DC-8 Inlet Characterization Experiment (DICE): Airborne versus surface sampling of mineral dust and sea salt aerosols, *Aerosol Sci. Technol.*, *41*, 136–159, doi:10.1080/02786820601118406.

Meloni, D., A. di Sarra, T. Di Iorio, and G. Fiocco (2005), Influence of the vertical profile of Saharan dust on the visible direct radiative forcing, *J. Quant. Spectrosc. Radiat. Transfer*, *93*, 397–413.

Müller, D., A. Ansmann, I. Mattis, M. Tesche, U. Wandinger, D. Althausen, and G. Pisani (2007), Aerosol-type-dependent Lidar ratios observed with Raman Lidar, *J. Geophys. Res.*, *112*, D16202, doi:10.1029/2006JD008292.

Nakajima, T., G. Tonna, R. Rao, P. Boi, Y. Kaufman, and B. Holben (1996), Use of sky brightness measurements from ground for remote sensing of particulate dispersion, *Appl. Opt.*, *35*, 2672–2686, doi:10.1364/AO.35.002672.

Niedermeier, D., F. Stratmann, H. Wex, E. Brüggemann, A. Kiselev, H. Henk, and H. Heintzenberg (2008), LACIS-measurements and parameterization of sea-salt particle hygroscopic growth and activation, *Atmos. Chem. Phys.*, *8*, 579–590, doi:10.5194/acp-8-579-2008.

Olmo, F. J., A. Quirantes, A. Alcántara, H. Lyamani, and L. Alados-Arboledas (2006), Preliminary results of a non-spherical aerosol method for the retrieval of the atmospheric aerosol optical properties, *J. Quant. Spectrosc. Radiat. Transfer*, *100*, 305–314.

Omar, A. H., J.-G. Won, D. M. Winker, S.-C. Yoon, O. Dubovik, and M. P. McCormick (2005), Development of global aerosol models using cluster analysis of Aerosol Robotic Network (AERONET) measurements, *J. Geophys. Res.*, *110*, D10S14, doi:10.1029/2004JD004874.

Osborne, S. R., J. M. Haywood, and N. Bellouin (2007), In situ and remote sensing measurements of the mean microphysical and optical properties of industrial pollution aerosol during ADRIEX, *Q. J. R. Meteorol. Soc.*, *133*, 17–32, doi:10.1002/qj.92.

Pappalardo, G., et al. (2004), Aerosol Lidar intercomparison in the framework of EARLINET project. 3. Raman Lidar algorithm for aerosol extinction, backscatter, and Lidar ratio, *Appl. Opt.*, *43*, 5370–5385, doi:10.1364/AO.43.005370.

Pedrós, R., V. Estellés, M. Sicard, J. L. Gómez-Amo, M. P. Utrillas, J. A. Martínez-Lozano, F. Rocadenbosch, C. Pérez, and J. M. Baldasano (2009), Climatology of the aerosol extinction-to-backscatter ratio from sun photometric measurements, *IEEE Trans. Geosci. Remote Sens.*, *48*, 237–249, doi:10.1109/TGRS.2009.2027699.

Petzold, A., and M. Schönlinner (2004), Multi-angle absorption photometry-A new method for the measurement of aerosol light absorption and atmospheric black carbon, *J. Aerosol Sci.*, *35*, 421–441, doi:10.1016/j.jaerosci.2003.09.005.

Pey, J., et al. (2008), Characterization of a long range transport pollution episode affecting PM in SW Spain, *J. Environ. Monit.*, *10*, 1158–1171, doi:10.1039/b809001g.

Quijano, A. L., I. N. Sokolik, and O. B. Toon (2000), Radiative heating rates and direct radiative forcing by mineral dust in cloudy atmospheric conditions, *J. Geophys. Res.*, *105*(D10), 12,207–12,219, doi:10.1029/2000JD900047.

Quirantes, A., F. J. Olmo, H. Lyamani, and L. Alados-Arboledas (2008), Correction factor for total scatter/backscatter nephelometer, *J. Quant. Spectrosc. Radiat. Transfer.*, *109*, 1496–1503, doi:10.1016/j.jqsrt.2007.12.014.

Ramanathan, V., M. V. Ramana, G. Roberts, D. Kim, C. Corrigan, C. Chung, and D. Winker (2007), Warming trends in Asia amplified by brown cloud solar absorption, *Nature*, *448*, 575–578, doi:10.1038/nature06019.

Santese, M., F. De Tomasi, and M. R. Perrone (2008), Advection patterns and aerosol optical and microphysical properties by AERONET over south-east Italy in the central Mediterranean, *Atmos. Chem. Phys.*, *8*, 1881–1896, doi:10.5194/acp-8-1881-2008.

Schmid, B., et al. (2006), How well do state-of-the-art techniques measuring the vertical profile of tropospheric aerosol extinction compare?, *J. Geophys. Res.*, *111*, D05S07, doi:10.1029/2005JD005837.

Shifrin, K. S. (1995), Simple relationships for the Angström parameter of disperse systems, *Appl. Opt.*, *34*, 4480–4485, doi:10.1364/AO.34.004480.

Sicard, M., C. Pérez, F. Rocadenbosch, J. M. Baldasano, and D. García-Vizcaíno (2006), Mixed-layer depth determination in the Barcelona coastal area from regular Lidar measurements: Methods, results and limitations, *Boundary Layer Meteorol.*, *119*, 135–157, doi:10.1007/s10546-005-9005-9.

Sicard, M., et al. (2009), Aerosol Lidar intercomparison in the framework of SPALINET-the SPAnish Lidar NETwork: Methodology and results, *IEEE Trans. Geosci. Remote Sens.*, *47*, 3547–3559, doi:10.1109/TGRS.2009.2021525.

Smirnov, A., B. N. Holben, T. F. Eck, O. Dubovik, and I. Slutsker (2000), Cloud-screening and quality control algorithms for the AERONET database, *Remote Sens. Environ.*, *73*, 337–349, doi:10.1016/S0034-4257(00)00109-7.

Smirnov, A., B. N. Holben, O. Dubovik, R. Frouin, T. F. Eck, and I. Slutsker (2003), Maritime component in aerosol optical models derived from Aerosol Robotic Network data, *J. Geophys. Res.*, *108*(D1), 4033, doi:10.1029/2002JD002701.

Sokolik, I. N., D. M. Winker, G. Bergametti, D. A. Gillette, G. Carmichael, Y. J. Kaufman, L. Gomes, L. Schuetz, and J. E. Penner (2001), Introduction to special section: Outstanding problems in quantifying the radiative impacts of mineral dust, *J. Geophys. Res.*, *106*, 18,015–18,027, doi:10.1029/2000JD900498.

Strapp, J. W., W. R. Leaitch, and P. S. K. Liu (1992), Hydrated and dried aerosol-size-distribution measurements from the Particle Measuring Systems FSSP-300 Probe and the Deiced PCASP-100X Probe, *J. Atmos. Oceanic Technol.*, *9*, 548–555, doi:10.1175/1520-0426(1992)009<0548:HADASD>2.0.CO;2.

Targino, A. C., K. J. Noone, and E. Öström (2005), Airborne in situ characterization of dry aerosol optical properties in multi-source influenced marine region, *Tellus, Ser. B*, *57*, 247–260.

Toledano, C., V. E. Cachorro, M. Sorribas, A. Berjón, B. A. de la Morena, A. de Frutos, and P. Gouloub (2007), Aerosol optical depth and Ångström exponent climatology at 'El Arenosillo' AERONET site (Huelva, Spain), *Q. J. R. Meteorol. Soc.*, *133*, 795–807, doi:10.1002/qj.54.

Volckens, J., and T. M. Peters (2005), Counting and particle transmission efficiency of the aerodynamic particle sizer, *J. Aerosol Sci.*, *36*, 1400–1408, doi:10.1016/j.jaerosci.2005.03.009.

Weinzierl, B., A. Petzold, M. Esselborn, M. Wirth, K. Rasp, K. Kandler, L. Schütz, P. Koepke, and M. Fiebig (2009), Airborne measurements of dust layer properties, particle size distribution and mixing state of Saharan dust during SAMUM 2006, *Tellus, Ser. B*, *61*, 96–117.

Welton, E. J., J. R. Campbell, J. D. Spinhirne, and V. S. Scott (2001), Global monitoring of clouds and aerosols using a network of micro-pulse lidar systems, in *Lidar Remote Sensing for Industry and Environmental Monitoring*, edited by U. N. Singh, T. Itabe, and N. Sugimoto, pp. 151–158, SPIE, Bellingham, Wash.

Welton, E. J., K. J. Voss, P. K. Quinn, P. J. Flatau, K. Markowicz, J. R. Campbell, J. D. Spinhirne, H. R. Gordon, and J. E. Johnson (2002), Measurements of aerosol vertical profiles and optical properties during INDOEX 1999 using micropulse lidars, *J. Geophys. Res.*, *107*(D19), 8019, doi:10.1029/2000JD000038.

Won, J. G., S. C. Yoon, S. W. Kim, A. Jefferson, E. G. Dutton, and B. Holben (2004), Estimation of direct radiative forcing of Asian dust aerosols with Sun/sky radiometer and Lidar measurements at Gosan, Korea, *J. Meteorol. Soc. Jpn.*, *82*, 115–130, doi:10.2151/jmsj.82.115.

Xu, J., M. H. Bergin, X. Yu, G. Liu, J. Zhao, C. M. Carrico, and K. Baumann (2002), Measurement of aerosol chemical, physical and radiative properties in the Yangtze delta region of China, *Atmos. Environ.*, *36*, 161–173, doi:10.1016/S1352-2310(01)00455-1.

L. Alados-Arboledas, J. L. Guerrero-Rascado, H. Lyamani, F. J. Olmo, and F. Navas-Guzmán, Centro Andaluz de Medio Ambiente, Universidad de Granada, Fuentenueva s/n, E-18071 Granada, Spain. (rascado@ugr.es)

J. Andrey and M. Gil, Área de Investigación e Instrumentación Atmosférica, Instituto Nacional de Técnica Aeroespacial, E-28850 Torrejón de Ardoz, Spain.

A. Comerón, F. Rocadenbosch, and M. Sicard, Remote Sensing Laboratory, Institut d'Estudis Espacials de Catalunya, E-08034 Barcelona, Spain.

F. Molero and M. Pujadas, Centro de Investigaciones Energéticas, Medioambientales y Tecnológicas, E-28040 Madrid, Spain.

R. Pedrós, Departmento de Física de la Tierra y Termodinámica, Universidad de Valencia, E-46010 Valencia, Spain.

O. Serrano-Vargas, Área de Ensayos en Vuelo y Armamento, Instituto Nacional de Técnica Aeroespacial, E-28850 Torrejón de Ardoz, Spain.